LAWRENCE
LIVERMORE
NATIONAL
LABORATORY

UCRL-TR-214906

Tomographic Imaging of Upper Mantle P- and S-wave Velocity Heterogeneity Beneath the Arabian Peninsula

Yongcheol Park, Andrew Nyblade, Arthur Rodgers, Abdullah Al-Amri

August 30, 2005

This work was performed under the auspices of the U.S. Department of Energy by University of California, Lawrence Livermore National Laboratory under Contract W-7405-Eng-48.

Tomographic Imaging of Upper Mantle P- and S-wave Velocity Heterogeneity Beneath the Arabian Peninsula

Yongchoel Park, Andrew Nyblade
Geosciences Department, Pennsylvania State University

Arthur Rodgers
Earth Sciences Division, Lawrence Livermore National Laboratory

Abdullah Al-Amri
King Saud University, Riyadh, Saudi Arabia

Technical Report
August 31, 2005

Summary

We report the estimates of three-dimensional P- and S-wave velocity structure beneath the Arabian Peninsula estimated from travel time delay tomography. We have completed travel time measurements and inversion of a partial data set provided by King Abdulaziz City for Science and Technology (KACST). This study builds on previous work by Benoit et al. (2003) following the methods of VanDecar and Crosson (1990) and VanDecar (1991). Data were collected from the Saudi Arabian National Digital Seismic Network (SANDSN) operated by KACST. The network consists of 38 stations (27 broadband and 11 short-period). We augmented the KACST data with delay times measured from permanent Incorporated Research Institutions for Seismology (IRIS) stations in the region (RAYN, EIL and MRNI) and the 1996 Saudi Arabian PASSCAL Experiment. This study shows the inverted P- and S-wave models computed with the combined data with all three different seismic networks (KASCST, IRIS, and the 1996 Saudi Arabian PASSCAL experiment) with best coverage beneath the Arabian Shield.

Tomographic images reveal low velocity features in the upper mantle along a north-south line from the southern Asir region to the northeastern portion of the Arabian Shield.

Introduction

The Arabian Shield consists of late Proterozoic crystalline basement overlain by Tertiary and Quaternary volcanic rocks in some places. The break-up of the Arabian Plate from Africa initiated at about 30-35 Ma, with the formation of the Red Sea-Gulf of Aden rift system (Coleman and McGuire, 1988). Volcanism was widespread between 30 and 12 Ma, and uplift of the Arabian Shield occurred at about 13 Ma (Coleman and McGuire, 1988). The volcanism and uplift are thought to be related to the presence of hot upper mantle (Camp and Roobol, 1992). The uplifted Arabian shield contains two major features: one is the Makkah-Madinah-Nafud (MMN; Figure 1) volcanic line in the south and the other is the Ha'il-Rutbah Arch in the north. The MMN volcanic line, extending north-south, has been the major site of volcanism in Saudi Arabia over the past 10 Ma, and the Ha'il-Rutbah Arch has been the site of several periods of uplift (Camp and Roobol, 1992).

Plume models

Many scientists have studied East Africa and the Arabian Shield to understand the origin of the uplift and volcanism, and proposed models can be divided into 3 groups: (1) a single large plume model, (2) multi-plume model, and (3) the African Superplume (e.g. Camp and Roobol, 1992; Burke, 1996; Li and Romanowicz, 1996; Grand et al., 1997; Ebinger and Sleep, 1998; Ritsema et al., 1999; Genna et al., 2002). Ebinger and Sleep (1998) suggested a model of a single large plume based on the similar uplift ages and volcanism in many parts of Africa. They suggested that a single large plume impinged beneath the Ethiopian plateau around 45 Ma and plume material flowed laterally in pre-existing zones of lithospheric thinning. The single plume model would be revealed as a

shallow but broad low velocity zone in the upper mantle, with a narrow vertical low velocity zone underneath representing the plume tail.

Other studies have presented multi-plume models based on the relative temperature gradient across the MMN volcanic line and across the Ethiopian and East Africa Plateaus to the south of the Arabian Shield. This model suggests a narrow deep rooted upwelling of a mantle plume centrally located beneath the western part of the Arabian Shield (Camp and Roobol, 1992) and additional plumes under Ethiopia and Kenya. This model would produce localized low velocity zones in the upper mantle with multiple vertical low velocity zones representing the plume tails.

Still other studies (Li and Romanowicz, 1996; Grand et al., 1997; Ritsema et al., 1999; Genna et al., 2002) argue for the existence of a broad, deep seated plume originating at the core mantle boundary called the Africa Superplume. The Superplume would be revealed as a broad low velocity extending from the lower to upper mantle.

Method

To investigate upper mantle structure under the Arabian Shield, we have completed travel time measurement and inversion of the combined data set collected from KACST seismic network. We augmented the KACST data with delay times measured from permanent IRIS stations in the region (RAYN, EIL and MRNI) and the 1996 Saudi Arabian PASSCAL Experiment data set. Figure 1 shows the locations of seismic network used in this study. We computed travel time differences for two nearly co-located stations (AFFS and AFIF in Figure 1) between KACST and the 1996 Saudi Arabian PASSCAL Experiment in order to investigate possible bias between the data sets before combining all data obtained from different seismic experiments (Figure 2). We sorted events recorded on the common stations by back azimuths and distances and measured P-wave travel time residuals from arrival times subtracted by theoretical travel time. The trends

of the residuals with back-azimuth and distance are very similar and indicate no bias between the travel time residuals for the common stations.

The whole modeling procedure for inverting lateral seismic velocity perturbations is illustrated in Figure 3. We started with the selection and archiving of event (Figure 4) recorded on KACST, the 1996 Saudi Arabian PASSCAL experiment, and three IRIS broadband stations. The procedure requires teleseismic events with ray paths penetrating the study area from below. In the next step, we computed relative arrival time residuals using the multi-channel cross-correlation method (VanDecar and Crosson, 1990) to invert for a three-dimensional velocity model. In order to formulate inverse problem we calculated the partial derivatives along with the theoretical travel times through the reference one-dimensional velocity model.

We parameterized travel time slowness using a grid of knots comprised of 34 knots in depth, 56 knots latitude between 12.0 N° and 37.0 N° and 56 knots in longitude between 29.5 E° and 55.0 E° (Figure 5). The horizontal knot spacing is one third of degree, and the vertical knot spacing is 25 km in the inner region of seismic array (17.4 N°-30.7 N°, 35.5 E°-48.5 E°, and 0-200 km depth). We used the IASP91 model (*Kennett and Engdahl*, 1991) as initial model for the inversion, and velocity structures were imaged using the inversion method of VanDecar (1991).

Results

P-wave Tomography:

We used 401 earthquakes resulting in 3416 ray paths with P- and PKP-wave arrivals. The majority of the events are located in the western Pacific Rim between back azimuths of 15 and 150 degrees, but the events are distributed over a wide range of back azimuths (Figure 4a). The waveforms were filtered with a zero-phase two-pole Butterworth filter between 0.5 to 2 Hz, and relative P-wave travel time residuals were computed. During

the multi-channel cross-correlation (MCCC) procedure, three-second time window was selected from filtered data. Figure 6a shows an example of filtered P-wave data aligned on the initial picking time. We plotted the relative arrival-time residuals versus back-azimuth and on station map for all events and stations to remove outliers, which may have resulted from cycle-skipping or GPS time errors, since least-squares inversions are sensitive to the presence of outliers.

In inversion procedure, VanDecar (1991) have chosen a 7-point finite element approximation to the Laplacian operator ($\nabla^2 s$) in order to penalize the roughness (second derivative) of the final slowness perturbation model and produce a smooth model. A final model can be determined by investigating the way in which changes in regularization levels (flattening and smoothing values), and this kind investigation is evaluated by the construction of a trade-off curve (Figure 7). For inverted model, 2000 iterations of the conjugate gradient procedure are performed with few different pair of flattening and smoothing values (Table 1), and Figure 7 is a plot of data fitting (% rms residual reduction) versus rms model roughness (s/km^3).

Table 1. Pairs of flattening and smoothing values used for constructing the trade-off curve (Figure 7).

	Flattening	Smoothing
A2	200	400
C2	800	1600
D2	1600	3200
E2	3200	6400
F2	6400	12800
G2	12800	256000

We have chosen the inverted model with the values of 1600 for flattening and 3200 for smoothing (D2 in Table 1) as our final model from trade-off curve (Figure 7). Figure 8 shows depth slices (a-d) and vertical cross-sections (e and f). Preliminary interpretation of these features would suggest that low velocities beneath the Gulf of Aqaba and southern Arabian Shield and Red Sea are related to mantle upwelling and seafloor spreading. Low velocities beneath the northern Arabian Shield may be related to

volcanic centers. The low velocity feature near the eastern edge of the Arabian Shield and western edge of Arabian Platform are mysterious, but could be related to mantle flow effects near the interface of lithospheres of different thickness.

S-wave Tomography:

For the S-wave model, we used 201 earthquakes resulting in 1602 ray paths with S- and SKS-wave arrivals. Although the total number of rays for S-wave model is a half of the rays for the P-wave model, the event distribution shows better coverage of back azimuth (Figure 4b). The signal processing procedures for S-wave are exactly same as P-wave data, but traces are filtered with lower frequency band (0.04 to 0.1 Hz), relative arrival time residuals are computed by the multi-channel cross-correlation (MCCC) method with fifteen-second time window. As a result we could use the short-period stations for the P-wave analysis, but were limited to the broadband stations for the S-wave modeling. Figure 5b shows an example of filtered S-wave data aligned on the initial picking time. We also plotted the relative arrival-time residuals versus back-azimuth and on station map for all S events and stations to remove outliers. The final model for S wave was inverted with same flattening and smoothing parameters with the values for P-wave model (D2 in table 1). Figure 9 shows depth profiles (a-d) and vertical cross-sections (e and f) of inverted S-wave velocity structure. The first order observations of velocity heterogeneities observed in depths through the P wave velocity models are confirmed by depth profiles of independently inverted S-wave model.

Resolution tests

To test the resolution of our P- and S-wave model, we produced a synthetic checkerboard model consisting of 100 km diameter spheres with ±5% slowness anomaly placed at 100, 400, and 700 km depths (Figure 10 and 11). Ray paths through a 1-D reference mode as defined by the IASP91 are used, and noise is added to the synthetic

travel-times as a Gaussian residual time error by a standard deviation of 0.02 and 0.04s for the P and S wave data, respectively. Figure 10 and 11 show the recovered structure from the checkerboard test for P- and S-wave velocity perturbations, respectively. The input spheres are retrieved below 200 km depth (Figure 10e-h for P-wave tomography, and Figure 11e-h for S-wave tomography), and the amplitudes of the slowness anomalies is recovered by ~20% of input anomaly. Since the spacing of seismic stations is sparse, and the ray paths of teleseismic body-waves are incident vertically near the surface, the velocity perturbations set at 100 km depth were recovered with very small anomaly values in our model. However the cross-section images of P- and S-wave models show that the pattern of the retrieved models are reliable between 200 km and 400 km depth (Figure 10g and h, and Figure 11g and h).

Conclusions

Ebinger and Sleep (1998) suggested that a model of a single large plume based on the similar uplift ages in Africa. They suggested that this single plume impinged beneath the Ethiopian plateau and plume material flowed laterally in pre-existing zones of lithospheric thinning (see the introduction). The major features of our models, however, are that a low velocity anomaly on the Southern part of the Arabian Shield in the upper mantle does not extend north of 21°N and dips to south (Figure 8 and 9). This structure is not consistent with the single plume model of Ebinger and Sleep (1998). Our model support multi plume model which is that there are two, separated plumes beneath the Arabian Shield (*Camp and Roobol*, 1992; *Burke*, 1996), and the lower velocity zones (higher temperature zones) are related with volcanic activities and topographic characteristics on the surface of the Arabian Shield.

Future work will investigate upper mantle structure under the Arabian Shield and the Red Sea using surface wave tomography. Body wave tomography has limited vertical resolution, but reasonable horizontal resolution (Figure 10 and 11). In contrast, surface wave tomography can give better vertical resolution but the horizontal resolution is not as

good. Although total velocity sensitivity of surface wave velocity is distributed over a broad depth range, peak sensitivity appears at a depth of approximately one third of the wavelength. By combining the results from body and surface wave tomography, we should be able to map the spatial and depth extent of anomalies in the upper mantle.

Acknowledgements

This work was performed under the auspices of the U.S. Department of Energy by University of California Lawrence Livermore National Laboratory under contract No. W-405-Eng-48. This is LLNL contribution UCRL-TR-??????.

References

Benoit, M. H., A. A. Nyblade, J. C. VanDecar, and H. Gurrola, 2003, Upper mantle P wave velocity structure and transition zone thickness beneath the Arabian Shield, *Geophysical Research Letters*, *30*.

Burke, K., 1996, The African Plate, *S. Afr. J. Geol.*, *99*, 341-409.

Camp, V. E., and M. J. Roobol, 1992, Upwelling Asthenosphere Beneath Western Arabia And Its Regional Implications, *Journal Of Geophysical Research-Solid Earth*, *97*, 15255-15271.

Coleman, R. G., and A. V. McGuire, 1988, Magma Systems Related To The Red-Sea Opening, *Tectonophysics*, *150*, 77-100.

Ebinger, C. J., 1989, Tectonic Development Of The Western Branch Of The East-African Rift System, *Geological Society Of America Bulletin*, *101*, 885-903.

Ebinger, C. J., and N. H. Sleep, 1998, Cenozoic magmatism throughout east Africa resulting from impact of a single plume, *Nature*, *395*, 788-791.

Kennett, B. and E. R. Engdahl (1991). Travel times for global earthquake location and phase identification, *Geophys. J. Int.,* 105, 429-465.

Grand, S. P., R. D. v. d. Hilst, and S. Widiyantoro, 1997, Global seismic tomography: A snapshot of convecton in the Earth, *GSA Today*, *7(4)*, 1-7.

Genna, A., P. Nehlig, E. Le Goff, C. Guerrot, and M. Shanti, 2002, Proterozoic tectonism of the Arabian Shield, *Precambrian Res.*, *117*, 21-40.

Li, X. D., and B. Romanowicz, 1996, Global mantle shear velocity model developed using nonlinear asymptotic coupling theory, *Journal Of Geophysical Research-Solid Earth*, *101*, 22245-22272.

Ritsema, J., H. J. van Heijst, and J. H. Woodhouse, 1999, Complex shear wave velocity structure imaged beneath Africa and Iceland, *Science*, *286*, 1925-1928.

VanDecar, J. C., and R. S. Crosson, 1990, Determination Of Teleseismic Relative Phase Arrival Times Using Multi-Channel Cross-Correlation And Least-Squares, *Bulletin Of The Seismological Society Of America*, *80*, 150-169.

VanDecar, J. C., 1991, Upper mantle structure of the Cascadia subduction zone from non-linear teleseismic travel time inversion, Ph. D. Thesis thesis, Univ. of Washington, Seattle, WA.

Figure captions

Figure 1. Location map of the study area and seismic stations. (BB, Broad-band station; SP, Short Period station)

Figure 2. Plot of travel-time residuals, subtracted by theoretical travel time computed with IASP91 model, (a) with back azimuths of events, and (b) great circle distances of events.

Figure 3. Flow chart of data reduction and travel-time inversion procedures.

Figure 4. The distribution of earthquakes for (a) P wave (3416 rays from 401 events) and (b) S wave (1602 rays from 201 events) plotted by the equal distance projection. The color scale indicates magnitude of each event, the red solid lines show plate boundaries, and each circle represents 30 degree distance interval from the center of KACST seismic array.

Figure 5. Bandpass filtered seismic traces. Traces have been aligned with respect to a initial pick of (a) P wave and (b) S wave. All traces have been filtered with a zero phase Butterworth filter with corner frequencies of 0.5 – 2.0 Hz and 0.04 – 0.1 Hz for the P and S waves, respectively. The vertical dashed lines represent the time windows (3s for P waves and 15s for S waves) of data used in the multi-channel cross correlation procedure.

Figure 6. The parameterization used to represent slowness. Node range in depth from 0 to 1600 km, in latitude from 12° to 37° and in longitude from 29.5° to 55°. The squares indicate seismic stations used in this study. The yellow boxes represent expected maximum resolution area from this study.

Figure 7. Trade-off curve between relative arrival-time residual reduction and model roughness for P wave inversion. The indexes A2-G2 on the figure refer to varying smoothing and flattening parameters presented in Table 1. The dashed line indicates 96% RMS travel-time residual reduction computed from MCCC (VanDecar and Crosson, 1990).

Figure 8. Map of lateral variations in P-wave velocities relative to iasp91 (Kennet and Engdahl, 1991) at (a) 100, (b) 200, (c) 300, and (d) 400 km depth. The lines (A-A’ and B-B’) show the locations of vertical cross-sections (e and f). The contact of the Arabian Shield and Arabian Platform is indicated by the white line.

Figure 9. Map of lateral variations in S-wave velocities relative to iasp91 (Kennet and Engdahl, 1991) at (a) 100, (b) 200, (c) 300, and (d) 400 km depth. The lines (A-A’ and B-

B') show the locations of vertical cross-sections (e and f). The contact of the Arabian Shield and Arabian Platform is indicated by the white line.

Figure 10. Synthetic checker board resolution test for inverted P-wave model. (a) shows the 100 km depth profile of input model, and (b) and (c) show the cross sections located on (a). 100 km diameter spheres defined by Gaussian functions across their diameter of ±5% peak velocity anomaly are distributed in layers of depth 100, 400 and 700 km. (d), (e) and (f) are the 100, 400 and 700 km depth profiles inverted from input model, and (g) and (h) are the cross-sections.

Figure 11. Synthetic checker board resolution test for inverted S-wave model. (a) shows the 100 km depth profile of input model, and (b) and (c) show the cross sections located on (a). 100 km diameter spheres defined by Gaussian functions across their diameter of ±5% peak velocity anomaly are distributed in layers of depth 100, 400 and 700 km. (d), (e) and (f) are the 100, 400 and 700 km depth profiles inverted from input model, and (g) and (h) are the cross-sections.

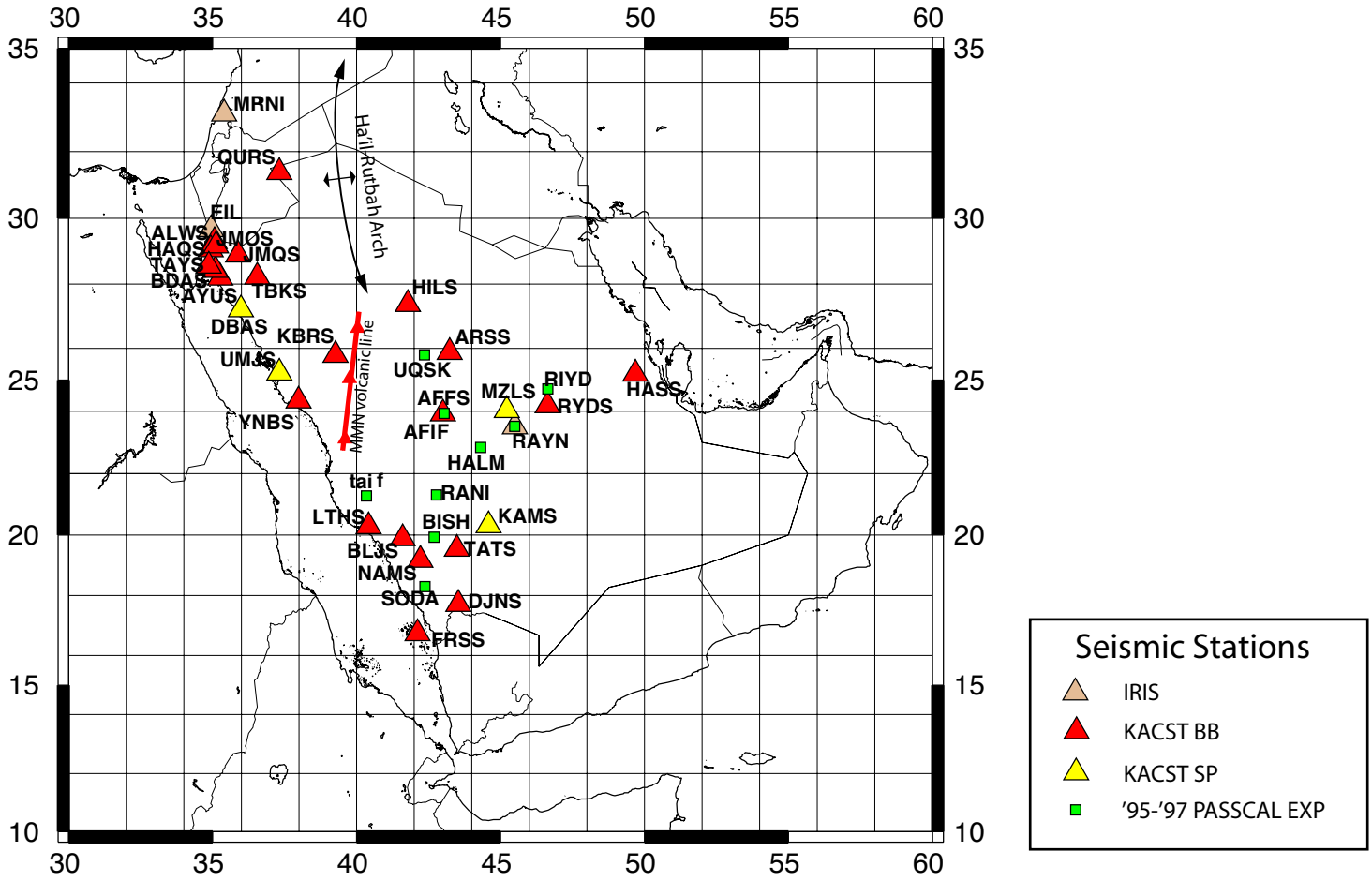

Figure 1. Location map of the study area and seismic stations. (BB, Broad-band station; SP, Short Period station)

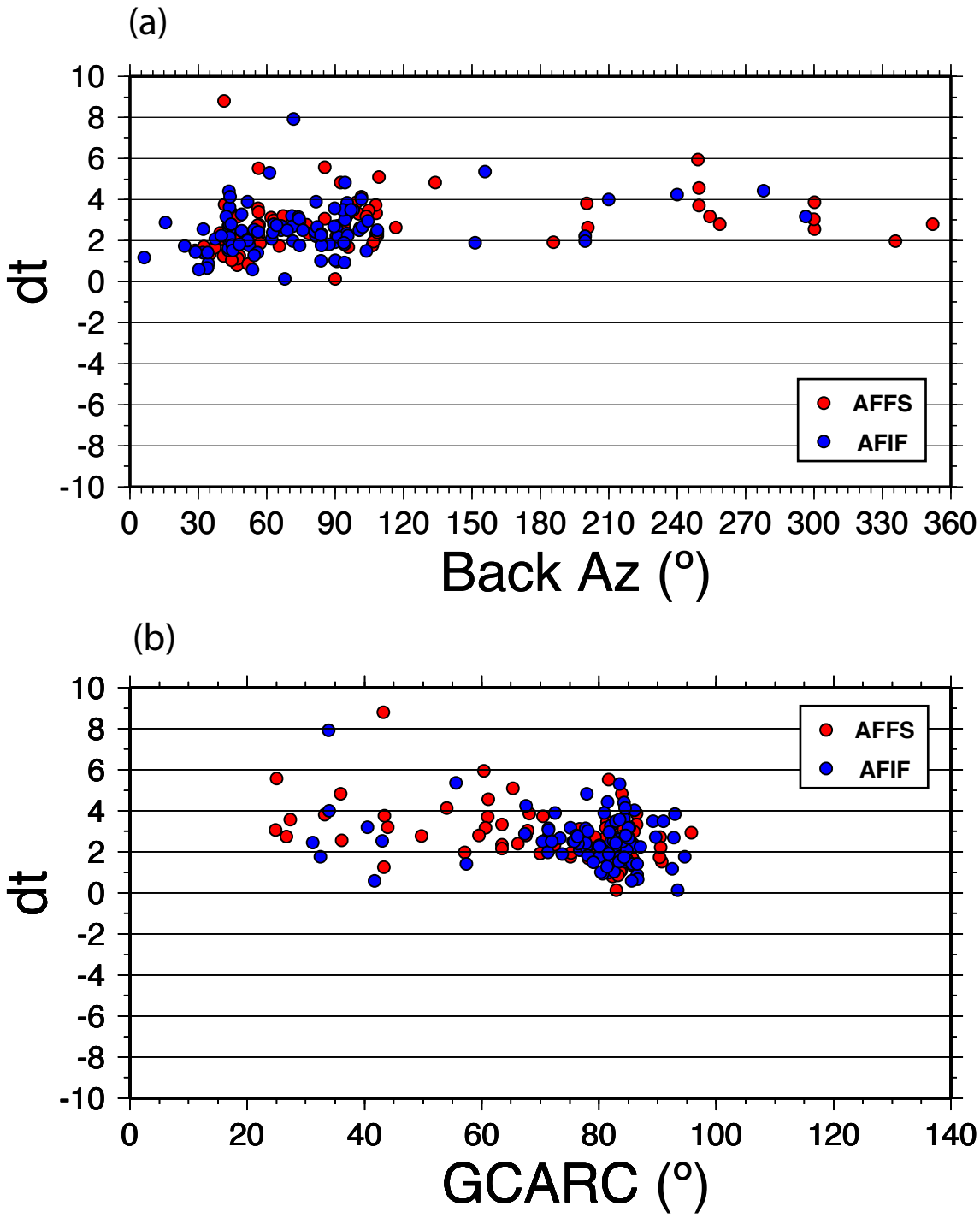

Figure 2. Plot of travel-time residuals, subtracted by theoretical travel time computed with IASP91 model, (a) with back azimuths of events, and (b) great circle distances of events.

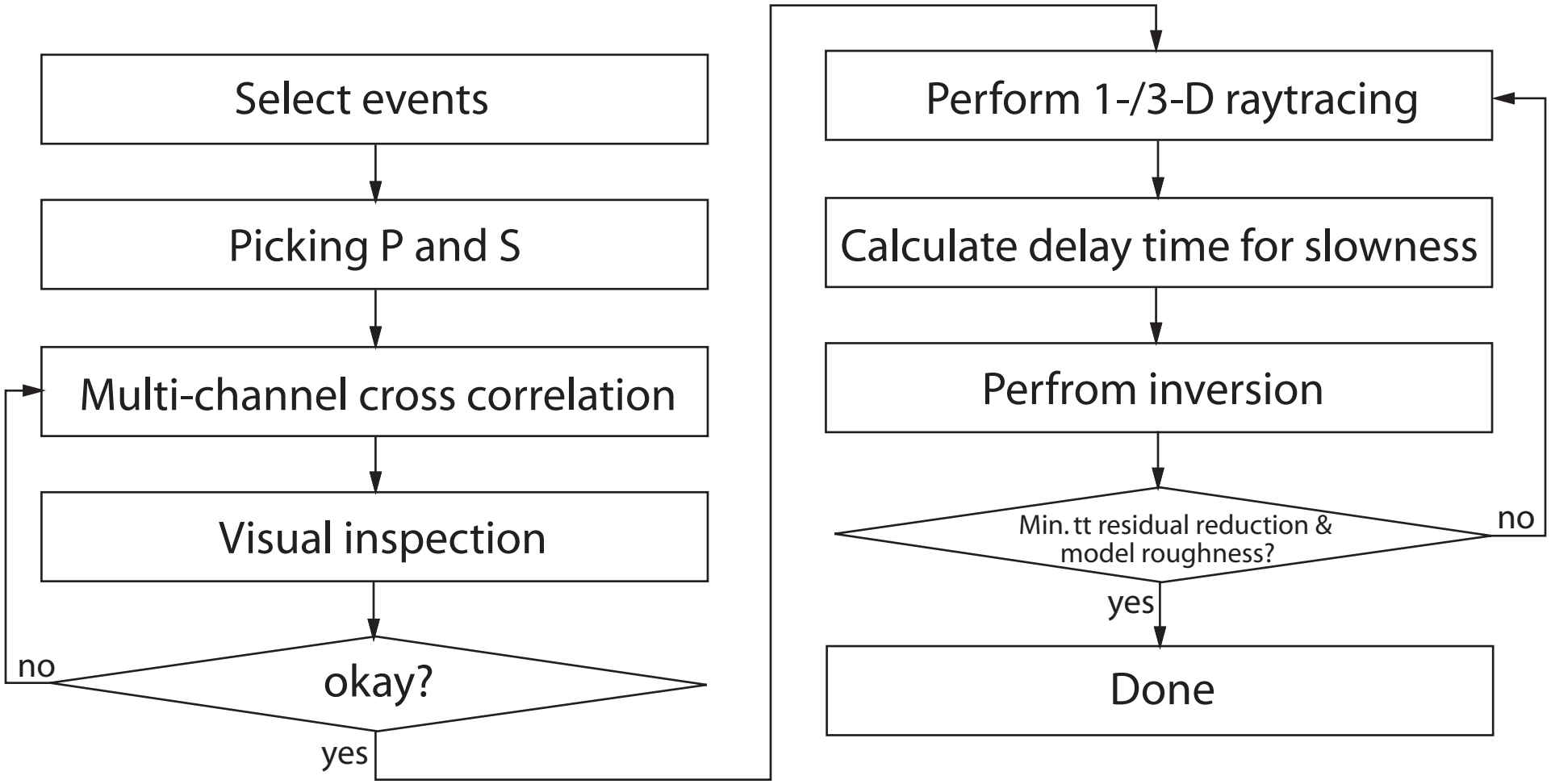

Figure 3. Flow chart of data reduction and travel-time inversion procedures.

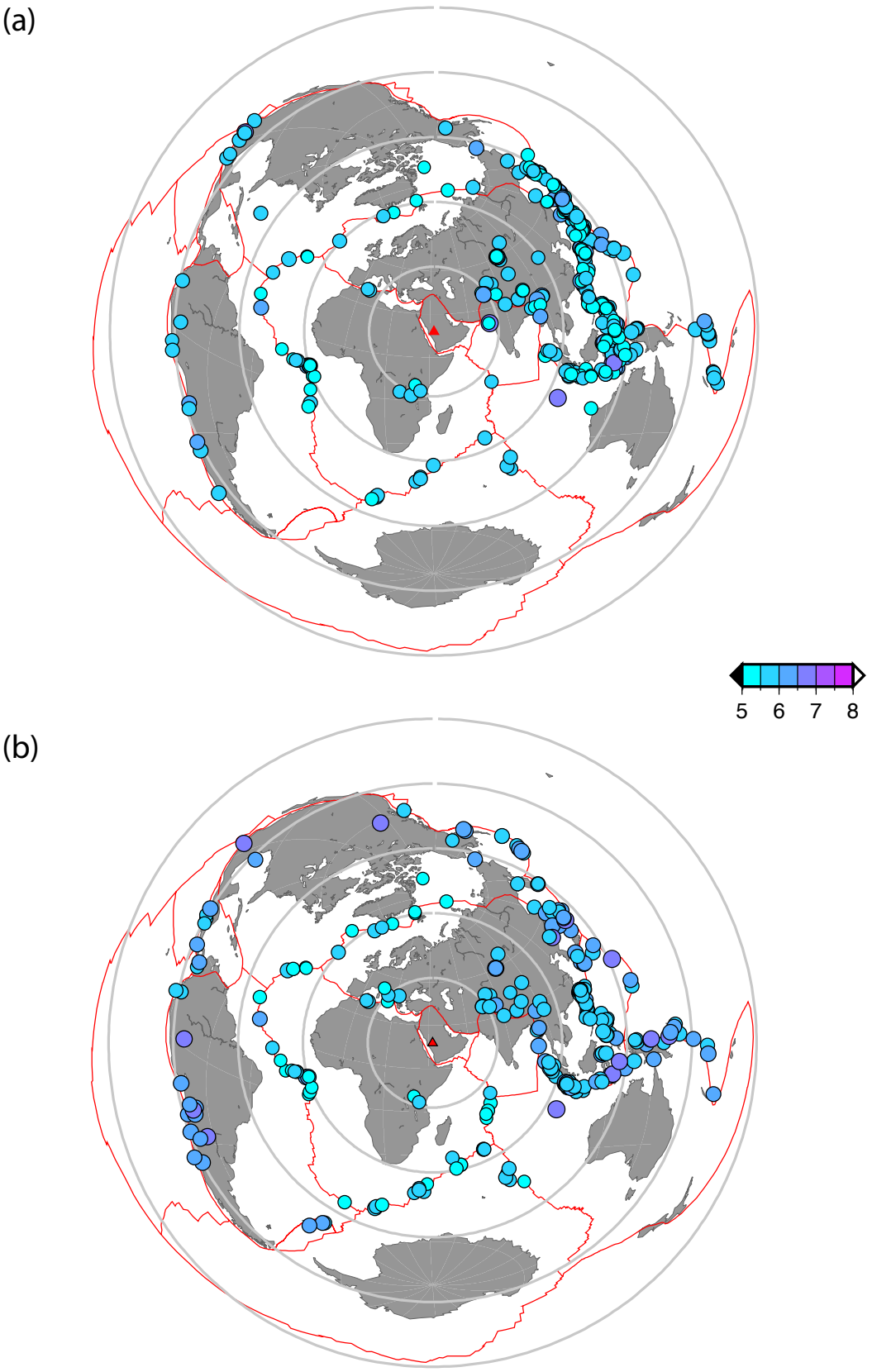

Figure 4. The distribution of earthquakes for (a) P wave (3416 rays from 401 events) and (b) S wave (1602 rays from 201 events) plotted by the equal distance projection. The color scale indicates magnitude of each event, the red solid lines show plate boundaries, and each circle represents 30 degree distance interval from the center of KACST seismic array.

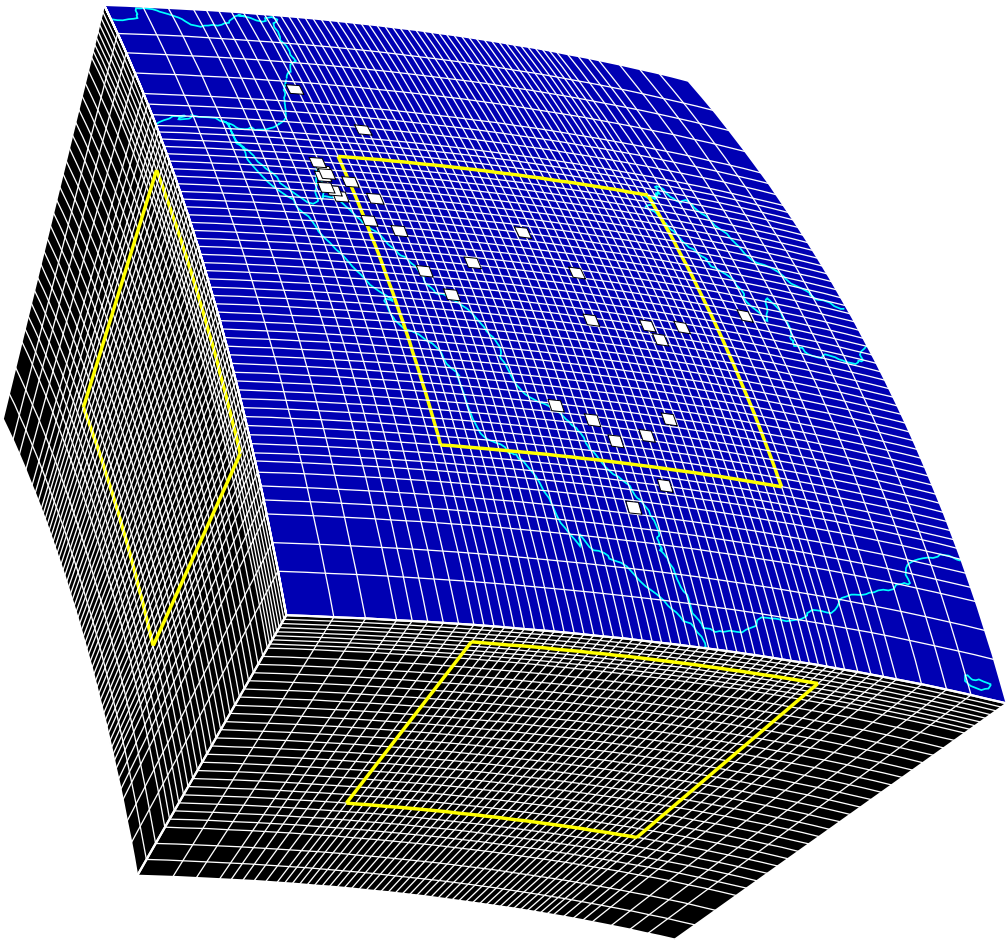

Number of knots in radius = 34; latitude = 56; longitude = 56

Total number of knots = 106624

Figure 5. The parameterization used to represent slowness. Node range in depth from 0 to 1600 km, in latitude from 12° to 37° and in longitude from 29.5° to 55°. The squares indicate seismic stations used in this study. The yellow boxes represent expected maximum resolution area from this study.

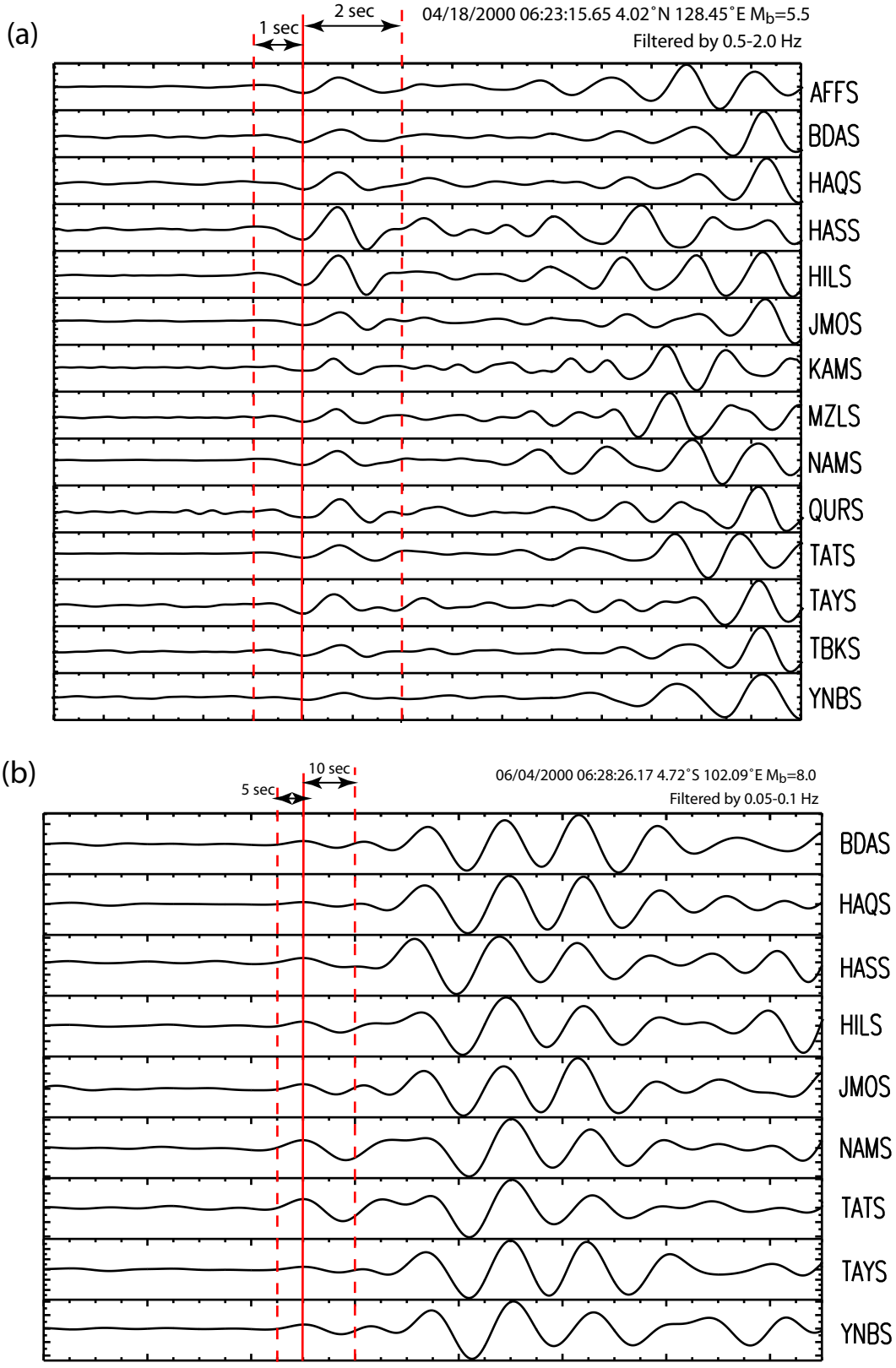

Figure 6. Bandpass filtered seismic traces. Traces have been aligned with respect to a initial pick of (a) P wave and (b) S wave. All traces have been filtered with a zero phase Butterworth filter with corner frequencies of 0.5 – 2.0 Hz and 0.04 – 0.1 Hz for the P and S waves, respectively. The vertical dashed lines represent the time windows (3s for P waves and 15s for S waves) of data used in the multi-channel cross correlation procedure.

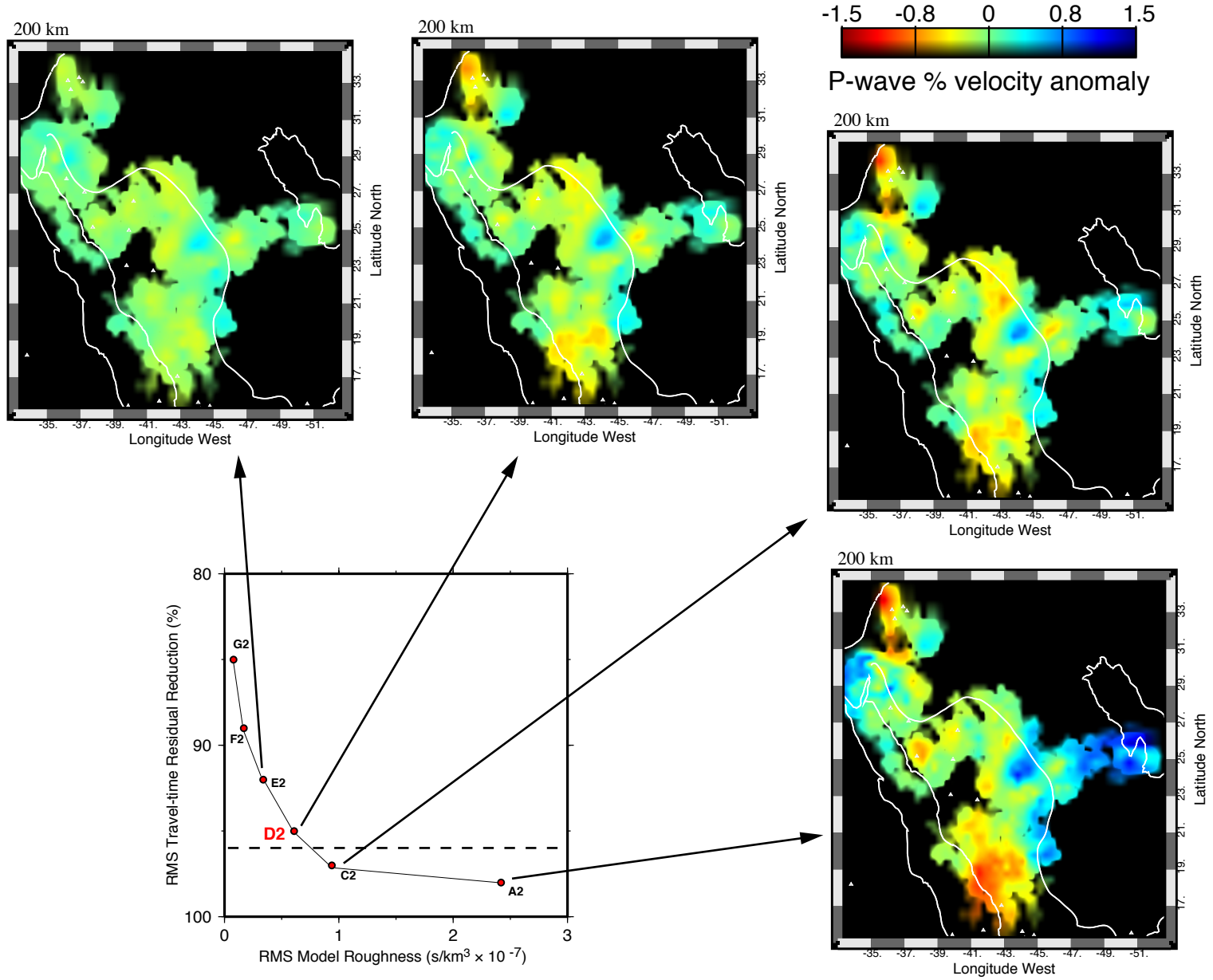

Figure 7. Trade-off curve between relative arrival-time residual reduction and model roughness for P wave inversion. The indexes A2-G2 on the figure refer to varying smoothing and flattening parameters presented in Table 1. The dashed line indicates 96% RMS travel-time residual reduction computed from MCCC (VanDecar and Crosson, 1990).

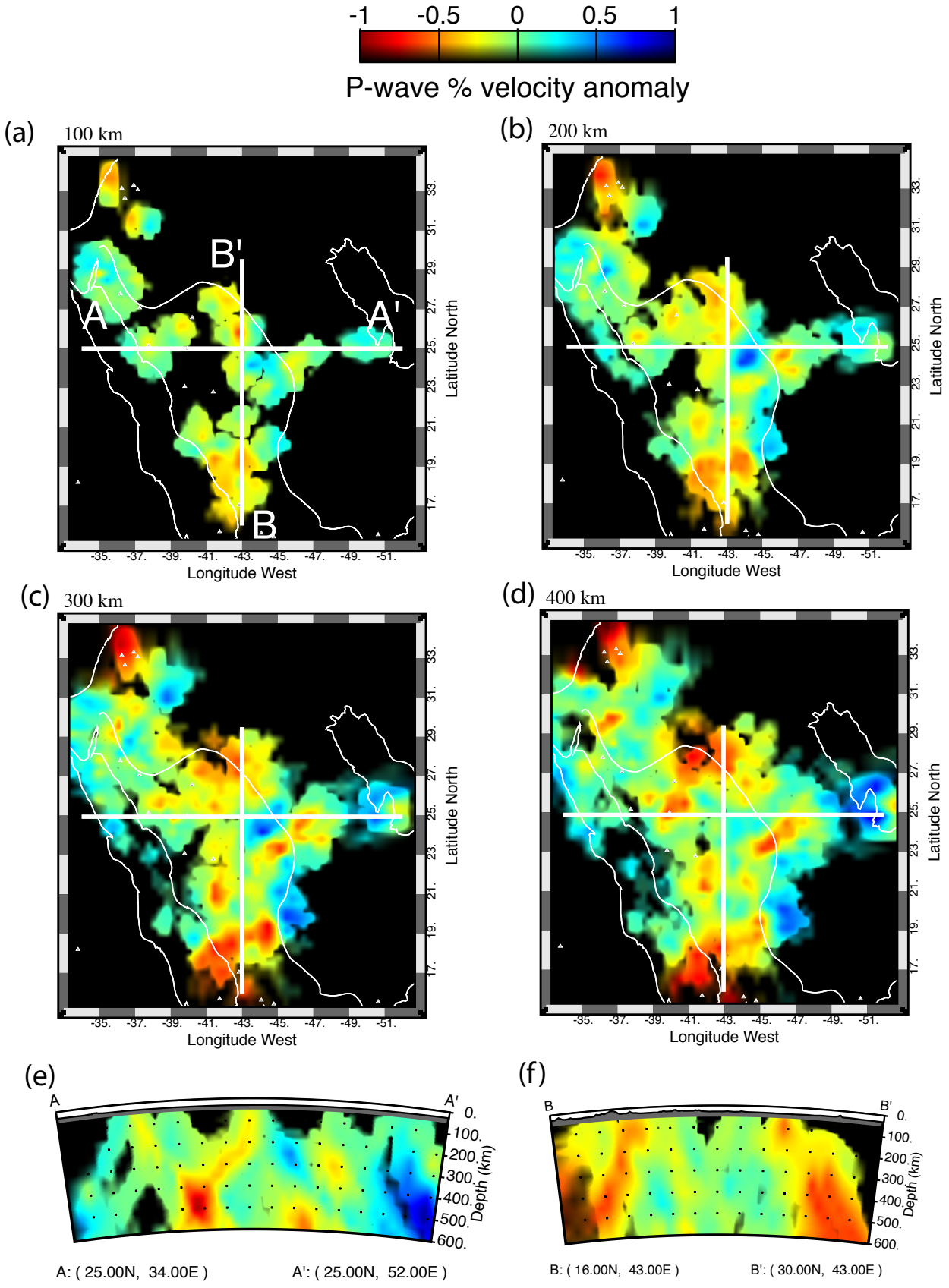

Figure 8. Map of lateral variations in P-wave velocities relative to iasp91 (Kennet and Engdahl, 1991) at (a) 100, (b) 200, (c) 300, and (d) 400 km depth. The lines (A-A' and B-B') show the locations of vertical cross-sections (e and f). The contact of the Arabian Shield and Arabian Platform is indicated by the white line.

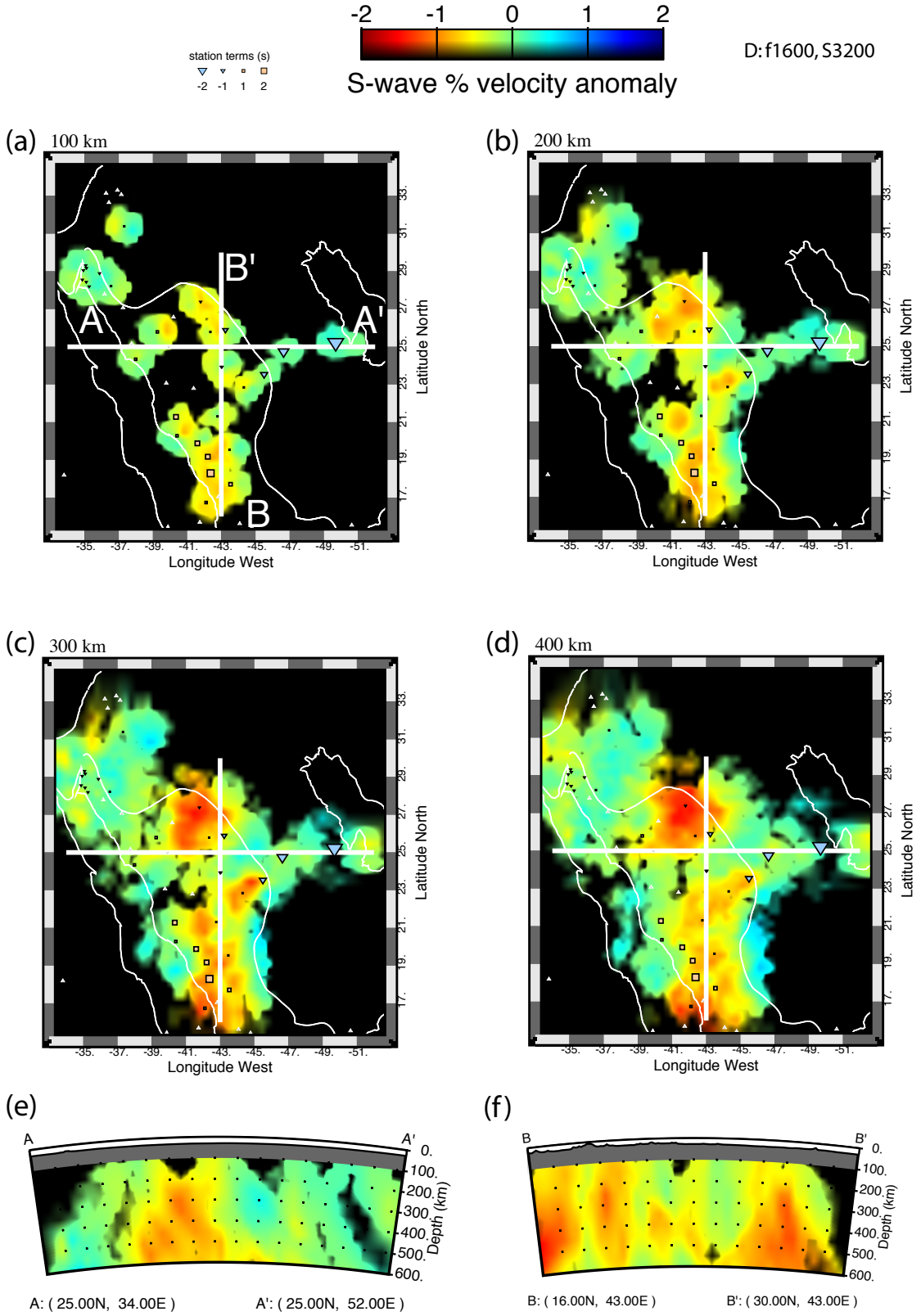

Figure 9. Map of lateral variations in S-wave velocities relative to iasp91 (Kennet and Engdahl, 1991) at (a) 100, (b) 200, (c) 300, and (d) 400 km depth. The lines (A-A′ and B-B′) show the locations of vertical cross-sections (e and f). The contact of the Arabian Shield and Arabian Platform is indicated by the white line.

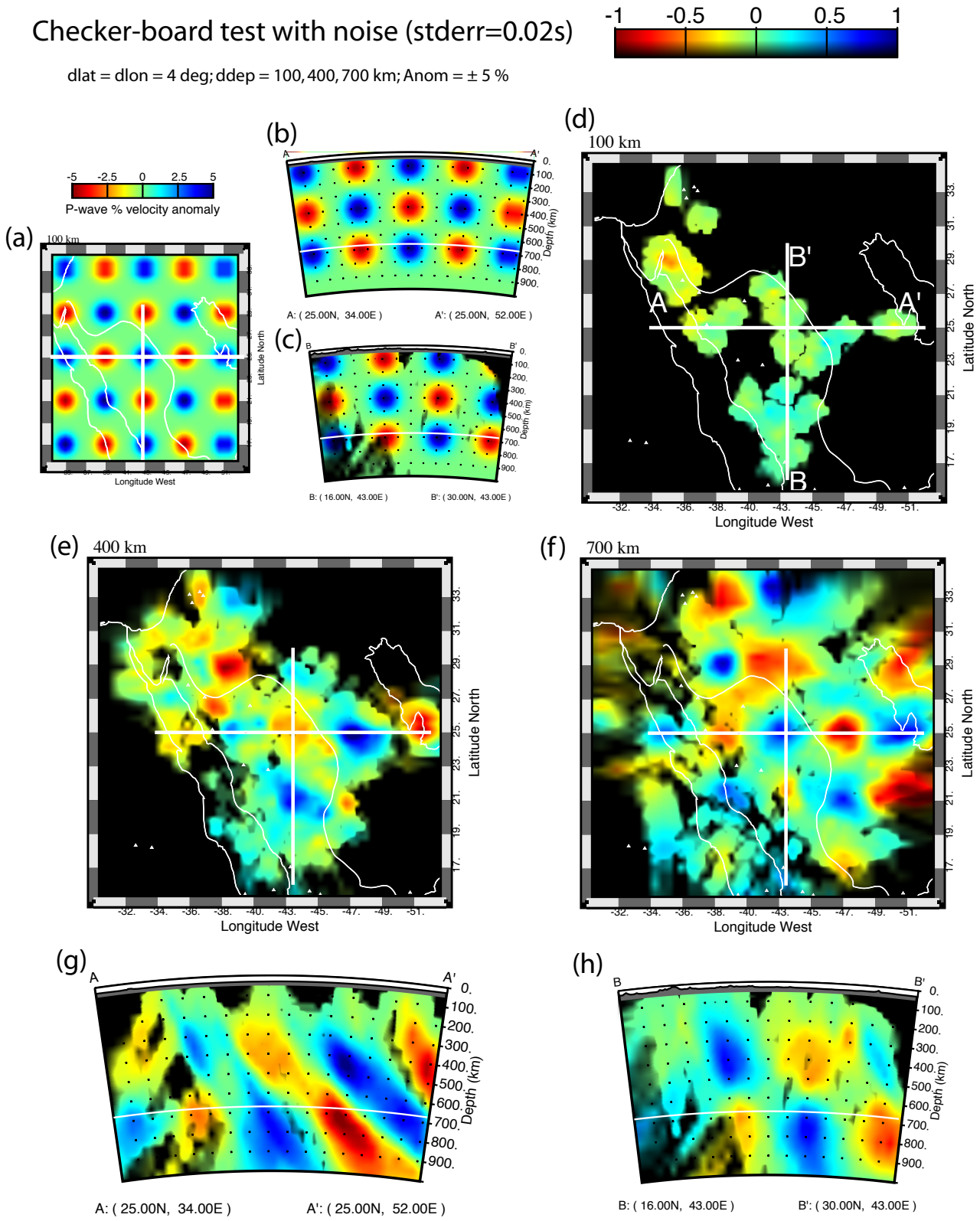

Figure 10. Synthetic checker board resolution test for inverted P-wave model. (a) shows the 100 km depth profile of input model, and (b) and (c) show the cross sections located on (a). 100 km diameter spheres defined by Gaussian functions across their diameter of ±5% peak velocity anomaly are distributed in layers of depth 100, 400 and 700 km. (d), (e) and (f) are the 100, 400 and 700 km depth profiles inverted from input model, and (g) and (h) are the cross-sections.

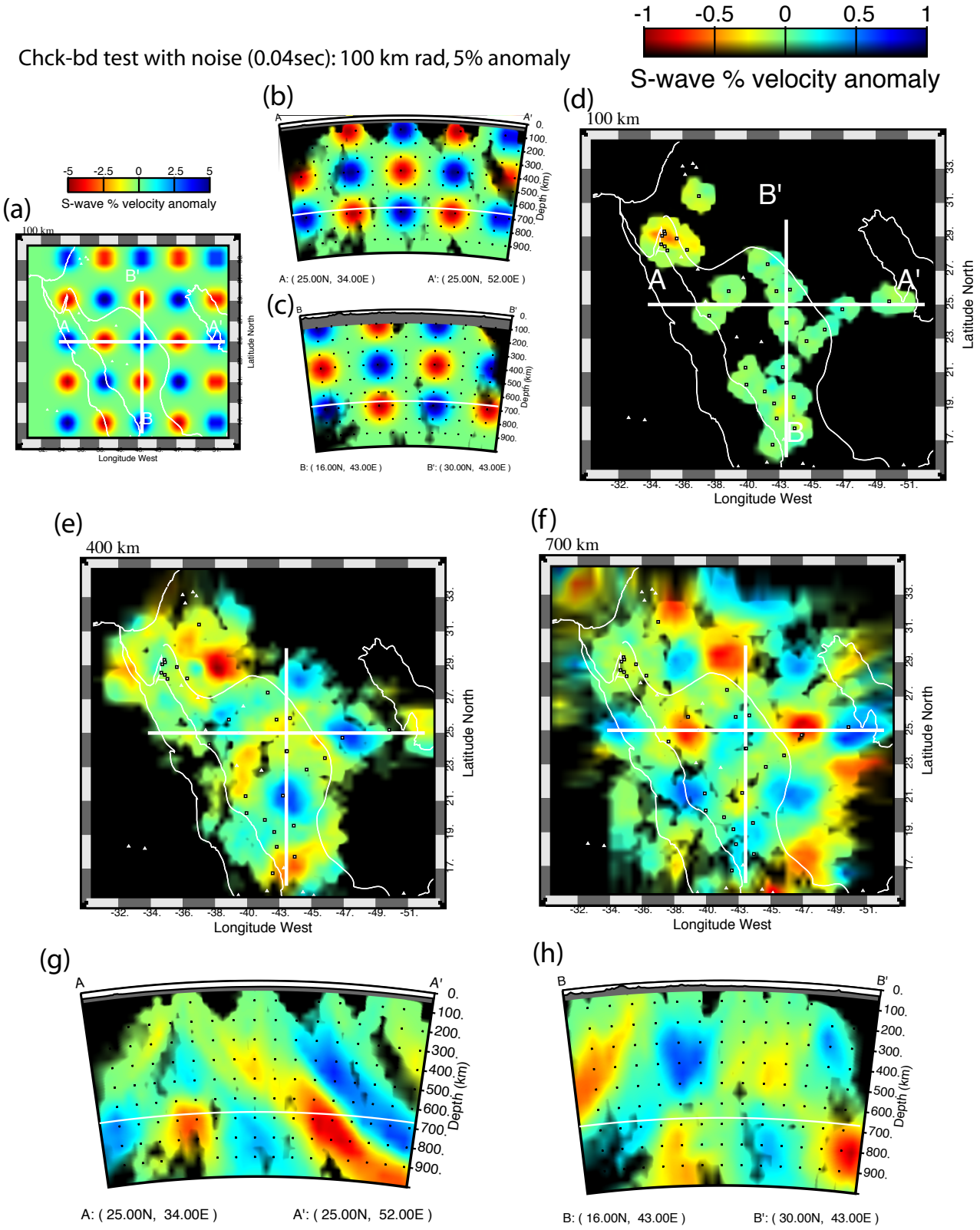

Figure 11. Synthetic checker board resolution test for inverted S-wave model. (a) shows the 100 km depth profile of input model, and (b) and (c) show the cross sections located on (a). 100 km diameter spheres defined by Gaussian functions across their diameter of ±5% peak velocity anomaly are distributed in layers of depth 100, 400 and 700 km. (d), (e) and (f) are the 100, 400 and 700 km depth profiles inverted from input model, and (g) and (h) are the cross-sections.